384 *Macromolecules* **2010**, *43*, 384–392
DOI: 10.1021/ma901921h

Macromolecules
ARTICLE

Crystal Orientation Effect on Electric Energy Storage in Poly(vinylidene fluoride-*co*-hexafluoropropylene) Copolymers

Fangxiao Guan,[†] Jilin Pan,[‡,⊥] Jing Wang,[†] Qing Wang,[‡] and Lei Zhu*[,†,§]

[†]*Polymer Program, Institute of Materials Science and Department of Chemical, Materials and Biomolecular Engineering, University of Connecticut, Storrs, Connecticut 06269-3136,* [‡]*Department of Materials Science and Engineering, Pennsylvania State University, University Park, Pennsylvania 16802, and* [§]*Department of Macromolecular Science and Engineering, Case Western Reserve University, Cleveland, Ohio 44106-7202.* [⊥]*Current address: College of Polymer Science and Engineering, Sichuan University, Chengdu 610065, People's Republic of China.*

Received August 30, 2009; Revised Manuscript Received October 9, 2009

ABSTRACT: By using different preparation and processing methods, poly(vinylidene fluoride-*co*-hexafluoropropylene) [P(VDF−HFP)] films with different crystal orientations were fabricated. Anisotropic dielectric properties and different electric energy storages were observed in these films. When the PVDF crystals in a film oriented with their *c*-axes perpendicular to the applied electric field, they exhibited large polarizability because the CF_2 dipole moments were randomly distributed in a plane parallel to the electric field. As a result, high dielectric constant and high electric energy density were achieved. On the contrary, when the crystal *c*-axes in a film oriented parallel to the electric field (or the CF_2 dipole moments perpendicular to the electric field), polarization became difficult. Consequently, low dielectric constant and low electric energy density resulted. The anisotropic polarizability was also displayed at high electric fields as evidenced by the difference in the remnant/maximum polarization and the dipole switching field for different crystal orientations. These results provide us a guidance to achieve optimal crystalline morphology in PVDF random copolymer films for high electric energy storage applications.

Introduction

Recently, there has been an increasing interest in utilizing ferroelectric polymers [e.g., poly(vinylidene fluoride) (PVDF)] for advanced dielectric applications, such as power conditioning, electric launch platform, and all electrical or hybrid vehicles, due to their large effective dielectric constants[1−5] and in turn high electrical energy storage.[6,7] Although both ferroelectric and linear dielectric polymers [e.g., biaxial oriented polypropylene (BOPP)] are insulating enough for advanced dielectric applications, their fundamental physics and thus electrical properties are fundamentally different. For example, BOPP is currently the state-of-the-art polymer capacitor film because of its high electric breakdown strength (730 MV/m at 63.2% Weibull failure probability and ∼600 MV/m at 1% Weibull failure probability for a test area of 2.0 cm^2)[8] and very low dielectric loss (< 0.0002 at 1 kHz).[9] Its electric energy density (U_e) can be described using a linear function: $U_e = \int E\, dD = 0.5\varepsilon_r\varepsilon_0 E^2$, where E is the electric field, D is the electric displacement, ε_r is the relative dielectric constant (2.2 for BOPP and independent of electric fields), and ε_0 is the vacuum permittivity.

PVDF and its random copolymers are well-known ferroelectric polymers that exhibit both high dielectric constant[1−4,10] and high dc breakdown strength (∼700 MV/m for ∼10 μm capacitor grade films).[6,11−13] However, their typical dielectric loss (tan δ) at 1 kHz is nearly 0.02 at ambient temperature because of electric dipole relaxation.[14] More importantly, they exhibit nonlinear dielectric and ferroelectric behaviors with nonlinear permittivity.[15,16] Relatively easy phase transformations between the paraelectric α-phase and ferroelectric phases (δ, γ, and β phases) at elevated electric fields[1,2] further enhance the cooperative ferroelectricity in PVDF crystals. Therefore, their stored and discharged U_e cannot be directly obtained from the ε_r in the above equation which is only valid for linear dielectrics (e.g., BOPP) because the ε_r is a function of the electric field and may exhibit a maximum at the coercive field (E_c).[15,17] In addition, the dielectric hysteresis often results in a significantly lower discharged U_e than the stored one.

To enable ferroelectric PVDF for advanced dielectric applications such as high energy density dielectric capacitors, modifications of PVDF have been pursuit to reduce its cooperative ferroelectricity in the crystals. For example, bulky comonomers such as chlorotrifluoroethylene (CTFE) or hexafluoropropylene (HFP) were randomly incorporated in PVDF, and the corresponding P(VDF−CTFE) or P(VDF−HFP) copolymers showed a high energy density of 17−25 J/cm^3 at ∼600 MV/m.[6,12] The high energy density is attributed to a relaxor ferroelectric behavior[18,19] achieved by the introduction of bulky −Cl atoms (or $-CF_3$ side groups) into the PVDF main chain to reduce the size of large α-form crystallites. However, the physical origin of the so-called relaxor ferroelectricity has not been well understood and quantified, and its relationships with different crystalline morphologies and different crystal orientations have yet to be elucidated. Recently, a low loss polymer, polystyrene (PS), was grafted to P(VDF−CTFE) using atom transfer radical polymerization.[20] After PVDF crystallization, PS formed a confining layer surrounding the PVDF lamellar crystals. As a result, less space charge was accumulated in the sample comparing to pure PVDF, and a much faster discharge was observed.

The origin of large polarization in PVDF and its copolymers is the strong and additive dipole moment perpendicular to the polymer chain in ferroelectric crystals. In δ-, γ-, and β-form crystals, the crystals possess net dipoles in their unit cells. Therefore, their polarizability is high when subjected to an external

*Corresponding author: e-mail lxz121@case.edu, Tel (216)368-5861.

 Published on Web 10/26/2009

electric field, and thus they exhibit high dielectric constants (e.g., 19.6 at 100 Hz for β-crystals).[21] In the α-form unit cell, neighboring dipole moments are in the opposite directions, and thus the crystal unit cell exhibits no net dipole. Therefore, its polarizability is low, and it exhibits a relatively low dielectric constant (e.g., 13 at 100 Hz).[14,21] Furthermore, the polarizability of PVDF crystals should depend on the orientation of dipole moments because the orientational polarization is more important than electronic and atomic polarizations in PVDF crystals.[22] We speculate that when the *c*-axis of the PVDF crystal is parallel to the electric field, all the dipole moments will distribute in a plane perpendicular to the electric field. Alignment of dipole moments with the electric field will be difficult, and thus the dielectric constant will be low and less electric energy can be stored in the crystal. When the *c*-axis of the PVDF crystal is perpendicular to the electric field, dipole moments will be distributed in a plane parallel to the electric field. Alignment of the dipole moments with the applied electric field will be relatively easy through either chain flipping or crank-shaft motions,[1] and thus the dielectric constant will be high and more electric energy can be stored in the crystals. However, the relatively high remnant polarization will prevent the release of energy.

Anisotropic dielectric properties have been reported in ceramic materials,[23] fluorinated polyimide and fluorinated poly(aryl ether),[24] poly(hexamethylene adipate),[25] and PVDF.[26,27] These materials showed different dielectric constants along different directions at low electric field. At high electric fields, however, the dielectric behavior was complicated by the possibility of electric field-induced phase transitions and nonlinear ferroelectricity.[28] Therefore, a clear understanding of the effect of crystal orientation on dielectric properties at high electric fields is indispensible for electric energy storage.

In this work, different crystal orientations were obtained for the same P(VDF−HFP) random copolymer by different film fabrication and processing conditions. Low dielectric constant and low electric energy storage were observed when PVDF crystalline lamellae were oriented parallel to the film, while high dielectric constant and high electric energy storage were obtained when the PVDF crystalline lamellae oriented perpendicular to the film. High electric field dielectric properties of the P(VDF−HFP) films having different crystal orientations were investigated by electric displacement−electric field hysteresis loops (i.e., *D*−*E* loops) and their derivative curves. Lower maximum and remnant polarization and a higher dipole switching field were observed in films where the PVDF crystalline lamellae were oriented parallel to the film than in those where PVDF crystalline lamellae oriented perpendicular to the film.

Experimental Section

Materials. P(VDF−HFP)-96/4 was purchased from Aldrich, which contained 4 mol % HFP comonomer as determined by proton nuclear magnetic resonance. Tetrahydrofuran (THF, Aldrich, HPLC grade) were used as received without further purification.

Film Fabrication and Processing. Film A with a thickness around 15 μm was prepared by slow solution-casting from 4 wt % THF solution at room temperature. Film B with a thickness around 8 μm was prepared by uniaxial stretching (~700% extension ratio) of a relatively thick (~50 μm) solution-cast and annealed (120 °C for 24 h) film at an elevated temperature (90 °C) using a home-built uniaxial stretching device. Film C with a thickness around 80−100 μm was prepared by melt-pressing the resin at 240 °C followed by immediate quenching into ice water. Thin film D with a thickness around 20 μm was prepared by uniaxial stretching (~700% extension ratio) of the film C at 130 °C.

Instrumentation and Characterization. Two-dimensional (2D) WAXD experiments were performed on an Oxford Xcalibur diffractometer with an ONYX CCD area detector. The X-ray wavelength was Cu Kα 0.1542 nm. One-dimensional (1D) WAXD profiles were obtained by integration from corresponding 2D WAXD images. The *d*-spacing was calibrated using silver behenate with the first-order reflection at a scattering vector $q = 1.076\ \mathrm{nm}^{-1}$, where $q = (4\pi \sin\theta)/\lambda$ (θ is the half scattering angle). Fourier transform infrared (FTIR) was performed on a Niclotet Magna 560 FTIR spectrometer. Differential FTIR spectra were obtained by subtracting different FTIR spectra with that for the P(VDF−HFP)-96/4 in the melt at 180 °C.[29] Differential scanning calorimetry (DSC) was performed on a TA DSC Q-20 with a scanning rate of 10 °C/min.

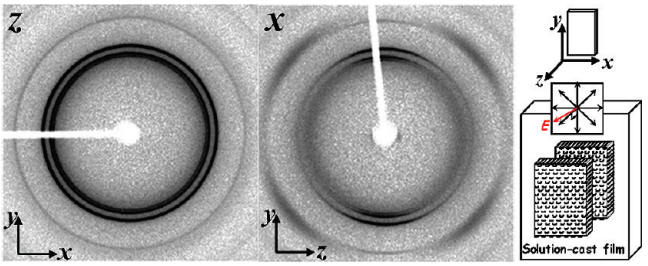

Figure 1. Two-dimensional (2D) WAXD patterns for the solution-cast film A. The X-ray beam was directed along the *z*- and *x*-directions, respectively. Crystal and dipole orientations are also shown in the schematic representation in the right panel.

The low field ε' and ε'' were measured using an Agilent 4284A Precision LCR meter. Polarization hysteresis loops at room temperature were collected using a modified Sawyer−Tower circuit at 10 Hz.[12] Gold electrodes were sputtered onto both surfaces of the film with a thickness around 50 nm. The gold electrode area was 5.0 cm^2 for the low field measurements and ca. 0.0531 cm^2 for the *D*−*E* loop measurements.

Results and Discussion

Characterization of Crystalline Morphology. Different crystal orientations in films A−D were studied by 2D WAXD, where the incident X-ray beam was directed along the *z* (normal to the film) and the *x* (perpendicular to the stretching direction and parallel to the film) directions, respectively. For the solution-cast film A, THF was chosen as the solvent because P(VDF−HFP) could crystallize from the solution after dissolution at a high temperature (e.g., 60 °C) and extended standing at room temperature during the slow solution-casting process. Afterward, the crystallized P(VDF−HFP) lamellar crystals lay parallel onto the substrate in the dried film (similar to single crystal mats). This was evidenced by sharp $(100)_\alpha$, $(020)_\alpha$, and $(110)_\alpha$ reflections oriented on the vertical *y*-direction in the *x*-uniaxial pattern in Figure 1. Note that the *x*-direction was arbitrarily chosen as parallel to the film because film A was never stretched. Sharp isotropic reflection rings were seen in the *z*-uniaxial pattern, indicating the lying-down lamellar crystals had a random orientation with respect to the normal direction of the film. Note that α-crystals exclusively dominated in the film and no β-crystals were observed, as evidenced by the 1D WAXD profile in Figure 2, where only $(100)_\alpha$, $(020)_\alpha$, and $(110)_\alpha$ reflections were seen at 12.45, 12.95, and 14.05 nm^{-1}, respectively. This is further confirmed by the differential FTIR spectrum in Figure 3. In the differential FTIR result, only α-form absorption bands were observed at 614, 532, 486, and 410 cm^{-1}, respectively [detailed peak assignment of FTIR absorption bands for α- and β-forms can be found in Table S1 in the Supporting Information].[30,31]

After solution-casting and uniaxial stretching, new crystalline morphology and phases developed in the film B in

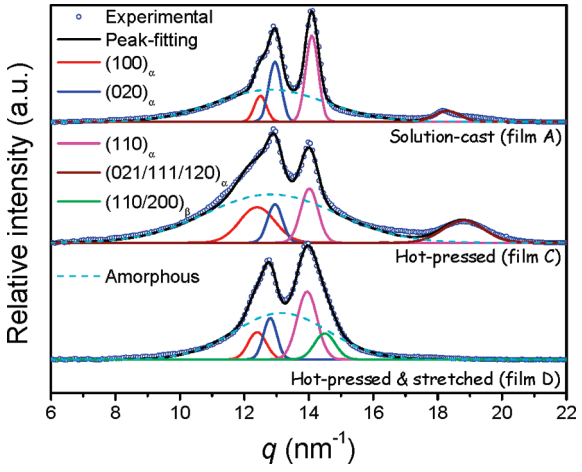

Figure 2. One-dimensional (1D) WAXD profiles for the solution-cast, hot-pressed, and hot-pressed and stretched films A, C, and D, respectively.

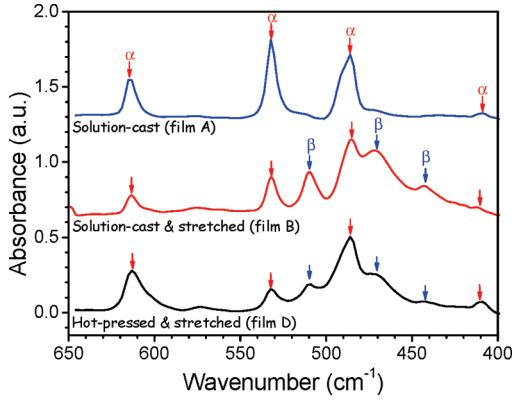

Figure 3. Differential FTIR absorption spectra for the solution-cast, solution-cast and stretched, and hot-pressed and stretched films A, B, and D, respectively.

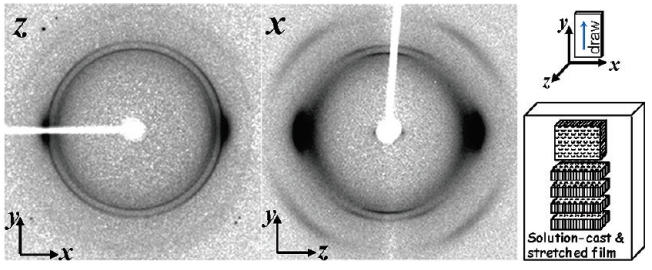

Figure 4. Two-dimensional (2D) WAXD patterns for the solution-cast and stretched film B. The X-ray beam was directed along the *z*- and *x*-directions, respectively. Crystal and dipole orientations are also shown in the schematic representation in the right panel.

addition to some pre-existing flat-on α-crystals, as evidenced in the WAXD patterns in Figure 4. For example, α-crystal reflections [$(100)_\alpha$, $(020)_\alpha$, and $(110)_\alpha$] with broad line widths were found in the horizontal *x*- and *z*-directions in the *z*- and *x*-uniaxial patterns, respectively. The orientation of these poor α-crystals was 90° apart from that of pre-existing large flat-on α-crystals, suggesting that part of the pre-existing flat-on α-crystals were pulled apart by uniaxial stretching and transformed into poor α-crystals with their *c*-axes parallel (or the crystalline lamellae transverse) to the drawing direction.[32] In addition, newly developed $(110)_\beta/(200)_\beta$ reflections with a broad line width oriented in the same

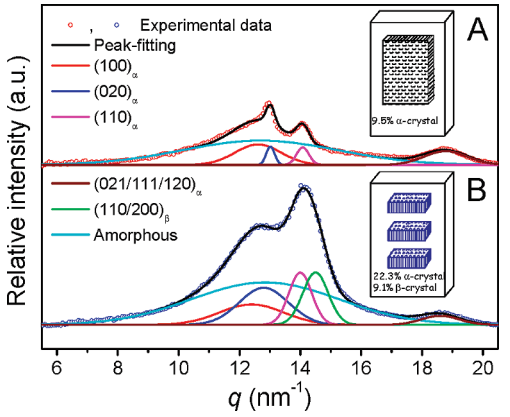

Figure 5. One-dimensional (1D) WAXD profiles for the solution-cast and stretched film B obtained by integration along (A) the *y*- and (B) the *z*-directions, respectively, when the X-ray beam is along the *x*-direction. The integration angle is ca. 50° around the *y*- and *z*-directions, respectively.

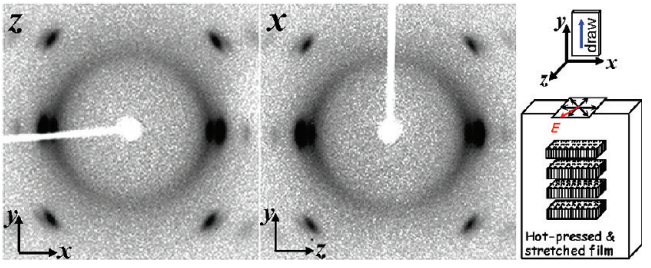

Figure 6. Two-dimensional (2D) WAXD patterns for the hot-pressed and stretched film D. The X-ray beam was directed along the *z*- and *x*-directions, respectively. Crystal and dipole orientations are also shown in the schematic representation in the right panel.

direction as those of the poor α-crystals, suggesting that poor *β*-crystals also oriented with their *c*-axes parallel to the drawing direction. The actual contents of these two crystal populations along the *y*- and *z*-directions were calculated from the corresponding 1D WAXD profiles (Figure 5) obtained from the *x*-uniaxial pattern in Figure 4. The results showed that there were 9.1% poor *β*-crystals and 22.3% poor α-crystals with their *c*-axes oriented parallel to the drawing direction and 9.5% large pre-existing α-crystals with their *c*-axes oriented perpendicular to the drawing direction. Further evidence for the existence of *β*-crystals was clearly seen in the differential FTIR spectrum in Figure 3 for the film B, where typical *β*-form absorption bands were observed at 510, 472, and 442 cm^{-1}. We conclude that these *β*-crystals must be transformed from the α-crystals under extensional stresses, which was often observed in literature.[33]

For the hot-pressed and stretched film D, there were well-oriented reflection arcs with broad line widths in the *z*- and *x*-uniaxial patterns in Figure 6. Broad line widths suggested that the crystallite sizes were small. Judging from the orientation of the $(100)_\alpha$, $(020)_\alpha$, and $(110)_\alpha$ reflections exclusively on the horizontal *x*- and *z*-directions [perpendicular to the drawing (*y*) direction], small PVDF crystals in the film D were aligned along the drawing direction. Moreover, extensional stresses also induced certain transformation of poor α-crystals into poor *β*-crystals. This was evidenced by the 1D WAXD profile in Figure 2 for the film D, where new $(110)_\beta/(200)_\beta$ reflections developed as a shoulder slightly beyond the $(110)_\alpha$ reflection, when compared with the 1D WAXD profile of the film C which possessed a pure α-phase.

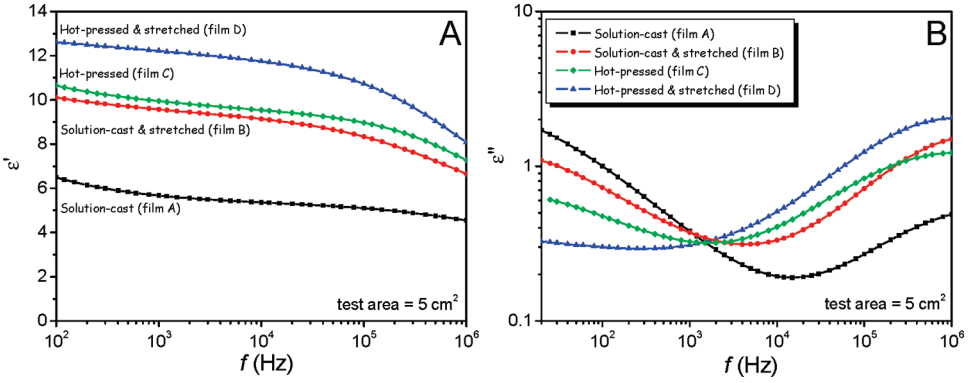

Figure 7. (A) Real part (ε') and (B) imaginary part (ε'') of the permittivity as a function of frequency for the solution-cast, solution-cast and stretched, hot-pressed, and hot-pressed and stretched P(VDF−HFP) films A−D, respectively.

The existence of β-crystals again can be clearly seen in the differential FTIR spectrum in Figure 3 with typical β-form absorption bands at 510, 472, and 442 cm^{-1}. Different crystal orientations in the films A, B, and D are summarized in the cartoon representations in Figures 1, 4 and 6, respectively.

Because of the stretching-induced β-crystals in films B and D, it is desired to calculate their content relative to that of the α-crystals. Although differential FTIR spectra in Figure 3 showed distinct β- and α-form absorption bands, the relative β-to-α ratio could not be accurately obtained because the absolute absorption coefficients were not readily available and different α- and β-crystal orientations (especially in the film B) further complicated the absolute infrared absorption. Therefore, we resort to 1D WAXD profiles in Figures 2 and 5 to determine the β-crystal contents in films B and D. To avoid interference from different crystal orientations, 1D WAXD profiles were obtained from the *x*-uniaxial patterns for all films, where the X-ray beam was always directed perpendicular to the *c*-axes of PVDF crystals. Therefore, equal probabilities for the (*hk*0) reflections in both α- and β-crystals could be assumed as long as the crystals had a random orientation around the drawing direction. The actual contents of α- and β-crystals were directly determined by the α- and β-crystallinity obtained from peak-fitting results in Figures 2 and 5; 9.1% β-crystals and 31.8% α-crystals in the film B and 7.3% β-crystals and 32.9% α-crystals in the film D. The overall crystallinity calculated from 1D WAXD profiles generally agreed with that obtained from DSC (see Figure S1 and Table S2 in the Supporting Information). In both stretched films (B and D), the contents of β-crystals were much higher than the overall crystallinity increase after uniaxial stretching (<3% based on WAXD and DSC results), confirming the stress-induced phase transformation from α- to β-crystals.

Dielectric Properties at Low Electric Fields. For ceramic materials, it was reported that dielectric properties were anisotropic with respect to different crystal orientations.[23] This is also true for crystalline PVDF and its copolymers.[26,27] The ε' and ε'' were measured as a function of frequency for films A−D at a low electric field (bias voltage = 1 V), and the results are shown in Figure 7. The ε' decreased with increasing the frequency for all P(VDF−HFP) films (Figure 7A) because they are ferroelectric and nonlinear in nature. The solution-cast film A had the lowest ε' (~5.6 at 1 kHz) compared with other films. In this film, dipole moments of CF_2 in the crystals were distributed in a plane nearly perpendicular to the electric field (see Figure 1). Therefore, their orientational polarizability in the flat-on crystals was low because it was difficult for them to conform to the electric field. On the contrary, the dipole moments of CF_2 in PVDF crystals of the hot-pressed and stretched film D were randomly distributed in a plane parallel to the electric field (see Figure 6). Therefore, their orientational polarizability in the transverse crystals was large, and film D showed the highest ε' (~12.2 at 1 kHz). Because of the random dipole orientations (dipole moments both perpendicular and parallel to the electric field) in the hot-pressed film C, it showed an ε' (~9.9 at 1 kHz) in between those for films A and D. Solution-cast and stretched film B had mixed dipole orientations. The slightly lower ε' (~9.6 at 1 kHz) was probably due to the presence of 9.5% flat-on large α-crystals (see Figure 4).

The relaxation properties of P(VDF−HFP) films with different crystal orientations were studied by the frequency spectra of the imaginary permittivity, as shown in Figure 7B. The solution-cast film A, the solution-cast and stretched film B, and the hot-pressed film C showed two relaxation peaks at low (less than 20 Hz) and high frequencies (~1 MHz), respectively. The relaxation peaks must originate from typical molecular motions in PVDF α-crystals.[34] The relaxation peak at low frequencies (~1 Hz), the so-called α-relaxation, is related to the molecular motion accompanied by the change of dipole moment along the chain direction in α-crystals. In the solution-cast film A, all of the chains were aligned along the applied electric field, and thus it had the largest relaxation peak at the low frequency. Because a significant portion of flat-on α-crystals had transformed into transverse crystals, leaving only 9.5% flat-on α-crystals in the solution-cast and stretched film B, a weaker relaxation peak was observed at the low frequency. The hot-pressed film C had a random chain orientation and thus showed an even smaller relaxation peak at the low frequency. Finally, there was no relaxation peak below 10^3 Hz in the hot-pressed and stretched film D because all of the chains were aligned perpendicular to the electric field. At high frequency (~1 MHz), two molecular motions have been proposed to be responsible for the relaxation process. One is the so-called β-relaxation, which is related to the micro-Brownian motion of noncrystalline chain segments.[34] The other is related to the molecular motion on the amorphous/crystalline and the α/β or α/γ (if there is a β- or γ-phase in PVDF crystals) interfaces.[35] For the P(VDF−HFP) films with different crystal orientations, we speculate that the second reason should dominate and the relaxation peak amplitude could be determined by the total area of the interfaces. There were more interface areas in the hot-pressed and stretched film D than in films B and C because the film B had 9.5% flat-on

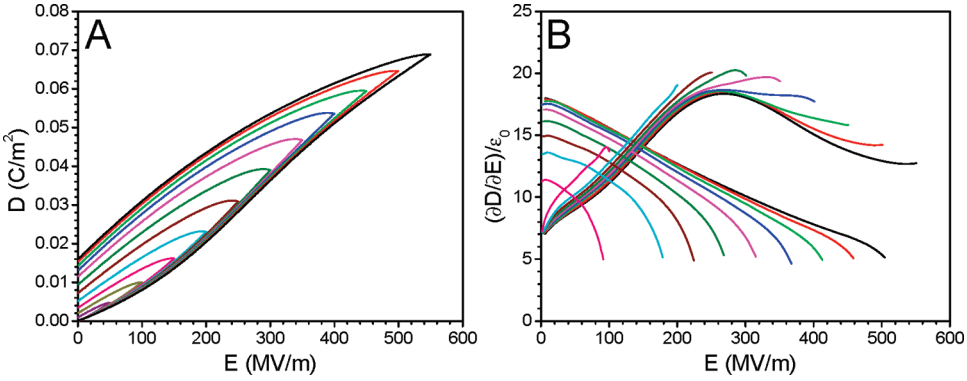

Figure 8. (A) Unipolar displacement−electric field ($D-E$) hysteresis loops for the solution-cast film A. The polarization electric field has an increment of 50 MV/m at each step up to 550 MV/m. (B) Derivative curves of D, $(\partial D/\partial E)/\varepsilon_0$, as a function of E for the solution-cast film A. The curves have the same color as their corresponding $D-E$ loops in (A).

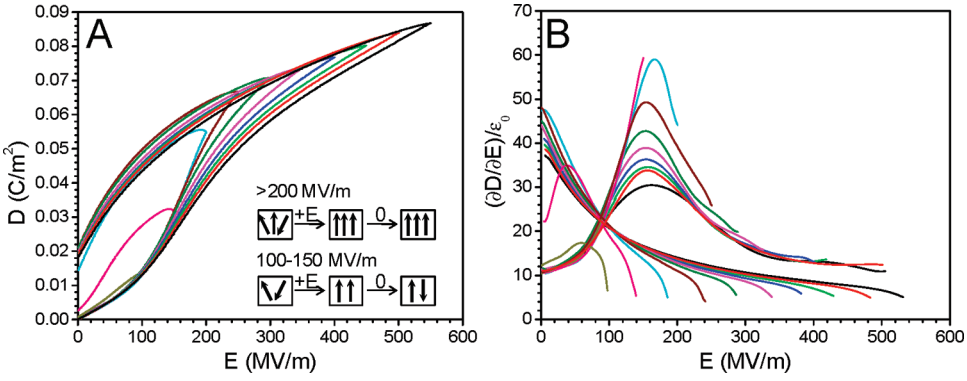

Figure 9. (A) Displacement−electric field ($D-E$) hysteresis loops for the solution-cast and stretched film B. The polarization electric field has an increment of 50 MV/m at each step up to 550 MV/m. (B) Derivative curves of D, $(\partial D/\partial E)/\varepsilon_0$, as a function of E for the solution-cast and stretched film B. The curves have the same color as their corresponding $D-E$ loops in (A).

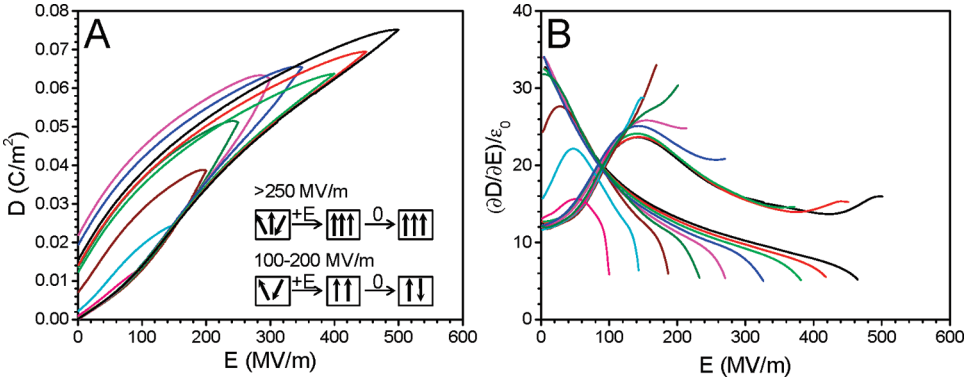

Figure 10. (A) Displacement−electric field ($D-E$) hysteresis loops for the hot-pressed and stretched film D. The polarization electric field has an increment of 50 MV/m at each step up to 500 MV/m. (B) Derivative curves of D, $(\partial D/\partial E)/\varepsilon_0$, as a function of E for the hot-pressed and stretched film D. The curves have the same color as their corresponding $D-E$ loops in (A).

large α-crystals and the film C had only α-crystals. Therefore, the film D had the highest relaxation peak at 1 MHz. Meanwhile, the solution-cast film A had only flat-on large α-crystals and thus the least interface area. Consequently, it had the smallest relaxation peak at 1 MHz.

Dielectric Properties at High Electric Fields. The dielectric properties of the P(VDF−HFP) films with different crystal orientations at high electric fields were studied by $D-E$ hysteresis loop measurements in Figures 8A, 9A, and 10A. Unipolar electric field was applied as a triangular waveform with a frequency of 10 Hz. For linear dielectric materials, the electric displacement can be related to the dielectric constant as the following:

$$\varepsilon_r = \frac{1}{\varepsilon_0}\frac{\partial D}{\partial E} \quad (1)$$

However, this relationship is generally invalid for a ferroelectric or nonlinear material such as PVDF because the electric displacement at high electric fields changes irreversibly with the electric field. Note that the electric displacement accounts for the dipole orientation (or polarization), while the dielectric constant reflects the motion (or the rate of change) of these dipoles. D and ε are not independent but

often correlate with each other. Although eq 1 cannot be directly used to calculate the field-dependent dielectric constant for nonlinear materials, it was observed experimentally that $(\partial D/\partial E)/\varepsilon_0$ qualitatively correlated with ε as a function of the electric field (see ref 15 and Figure S2 in the Supporting Information). In our $D-E$ loop measurements, unfortunately the field-dependent $\varepsilon(E)$ values could not be directly obtained. Therefore, $(\partial D/\partial E)/\varepsilon_0$ was used to qualitatively correlate with the dielectric constant at high electric fields for P(VDF−HFP) films with different crystal orientations. The corresponding results of $(\partial D/\partial E)/\varepsilon_0$ as a function of the electric field are shown in Figures 8B, 9B, and 10B. All of the differential curves in Figures 8B, 9B, and 10B have the same color as corresponding $D-E$ loop curves in Figures 8A, 9A, and 10A.

From the above results, the solution-cast film A only had flat-on α-crystals, which showed low orientational polarizability at low electric fields. At high electric fields, the low orientational polarizability was demonstrated by the low electric displacement and the high dipole switching field. For example, at an electric field of 500 MV/m, D was 0.065, 0.084, and 0.075 C/m^2 for the solution-cast film A, the solution-cast and stretched film B, and the hot-pressed and stretched film D, respectively. The peak position in the derivative curve of D in Figure 8B indicated that the fastest polarization reversal in the film A occurred at an electric field of 260 MV/m. This is much higher than typical coercive fields of 50−70 MV/m for β-PVDF[17] and ∼110 MV/m for α-PVDF[6] because the largest dipole moment of the α-crystals oriented in a plane perpendicular to the electric field for the film A. However, there is a small dipole moment along the chain direction in α-crystals, which usually have alternating (or random) up and down orientations for the up and down helices, respectively.[28] At high electric fields, these up and down dipoles could be poled into the same direction. We speculate that the maximum $(\partial D/\partial E)/\varepsilon_0$ in Figure 8 could be a result of poling these dipoles along the chains in α-crystals.

There are three types of crystal populations in the solution-cast and stretched film B; large face-on α-crystal and poor transverse α- and β-crystals. Upon poling, the dipole switching field appeared at 160 MV/m, when the polarization field reached at 200 MV/m and above (see Figure 9B). This was much lower than that for the solution-cast film A because the largest dipole moments in the sample oriented in a plane parallel to the applied field, rather than perpendicular to it. When the applied polarization field was relatively low (e.g., 150 and 200 MV/m), the maximum value of $(\partial D/\partial E)/\varepsilon_0$ was about 60 because most dipoles had randomized back to the original state during the previous depolarization (or discharge) cycle. When the unidirectional poling cycle continued to higher electric fields, more dipoles were poled (or saturated) and did not switch back to the original state upon removal of the electric field during the previous discharge cycle. Therefore, the maximum value of $(\partial D/\partial E)/\varepsilon_0$ kept decreasing. When the E reached 550 MV/m, $(\partial D/\partial E)/\varepsilon_0$ decreased to about 30.

Upon discharging, there was almost no hysteresis in the $D-E$ loop when the polarization field was less than 100 MV/m. When the polarization field reached 100 and 150 MV/m, half-propeller-shaped $D-E$ loops were observed, which could be attributed to an antiferroelectric-like behavior. Similar propeller-shaped $D-E$ loops with two-step dipole switching were also observed in P(VDF−trifluoroethylene) [P(VDF−TrFE)] copolymers with relatively low VDF contents at intermediate temperatures between the ferroelectric (β) and the paraelectric (rotating α) phases.[15,36−38] The first step switching corresponded to a fast depolarization process to a nonpolar (antiferroelectric) phase, and the second step was attributed to a slow repolarization process. We speculate that similar antiferroelectric-like behavior could exist in the solution-cast and stretched film B. At a relatively low poling field (e.g., 100−150 MV/m), almost no space charges were induced in the sample. After removal of the applied electric field, the depolarization field could drive the formation of a nonpolar (antiferroelectric or randomized) phase. This resulted in a low remnant polarization and a half-propeller-type $D-E$ hysteresis loop, as seen in Figure 9A. At the high poling fields (>200 MV/m), space charges were induced to stabilize the oriented dipoles, and the dipoles were thus saturated.[21,39−42] After removal of the applied electric field,

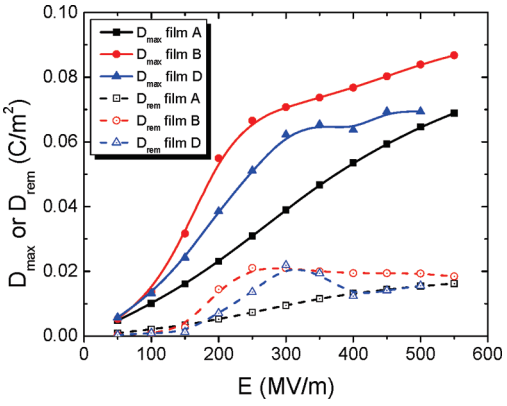

Figure 11. Maximum and remnant polarizations, D_{max} and D_{rem}, as a function of the electric field for films A, B, and D with different PVDF crystal orientations.

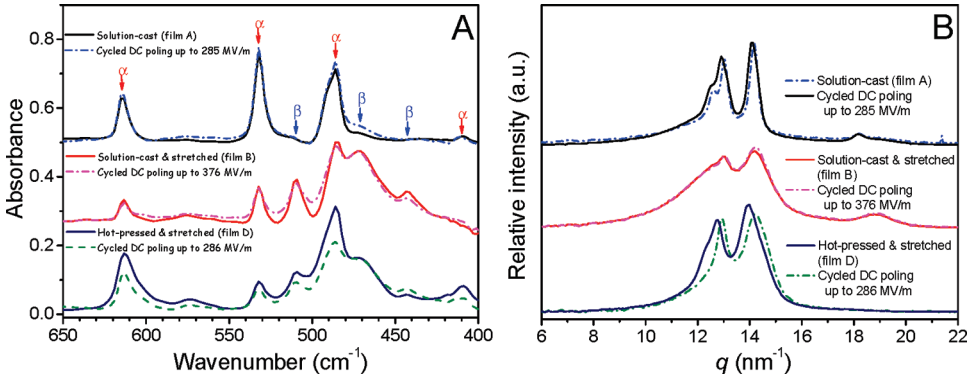

Figure 12. (A) Differential FTIR spectra and (B) 1D WAXD profiles for the solution-cast film A, solution-cast and stretched film B, and the hot-pressed and stretched film D before and after the cycled dc poling process, respectively.

the oriented dipoles preserved and thus resulted in a high remnant polarization. These are illustrated in the schematic inset in Figure 9A. Since the film B contained a certain amount of β-crystals, whose dipoles should be more mobile than the α-crystal dipoles, we speculate that the β-crystals could be responsible for the fast dipole switching upon removal of the applied field. For example, upon discharging, the fast dipole depolarization occurred at 38 MV/m for a poling field of 100 MV/m, and 58 MV/m for a poling field of 150 MV/m (see Figure 9B). To determine whether the fast depolarization step is related to the reorientation of the β-crystal dipoles or not, more experiments will be carried out in the future.

The hot-pressed and stretched film D had certain differences from film B. First, film B had smaller crystallite sizes in the transverse α- and β-crystals than film D. This can be seen by comparing the 1D WAXD profile for film D (Figure 2) and that for film B (Figure 5B), and the line widths of the reflections for the transverse α- and β-crystals for the film B were broader than those for film D. Second, film D did not have large flat-on α-crystals as in film B. Therefore, more crystal−amorphous interfacial areas were present in film D, and thus a stronger depolarization field resulted. Consequently, film D displayed somewhat different $D-E$ hysteresis loops (Figure 10A) from the film B (Figure 9A). For example, upon charging, the dipole switching field was 140 MV/m when the polarization field was above 300 MV/m (Figure 10B), slightly lower than that (160 MV/m) for film B. It is because of the stronger depolarization field in film D that more diminished macroscopic polarization in film D resulted than in film B, as we discussed before. Meanwhile, the maximum $(\partial D/\partial E)/\varepsilon_0$ was less than 25 (Figure 10B), smaller than those for film B at the same poling electric field.

Upon discharging, similar antiferroelectric-like behavior, as in film B, was observed for film D at a polarization electric field between 100 and 200 MV/m because half-propeller-shaped $D-E$ loops again were observed in Figure 10A. After removal of the applied electric field, the oriented dipoles could revert back to the nonpolar (antiferroelectric or random) phase because of its higher depolarization field. As a consequence, a low remnant polarization resulted. For example, the remnant polarization was 0.0075 C/m^2 for film D as compared to 0.014 C/m^2 for film B at a polarization field of 200 MV/m. The fast depolarization step was also evidenced by a peak in the $(\partial D/\partial E)/\varepsilon_0$ curves during the discharge process (see Figure 10B). Different from film B, film D showed a peak around 25 MV/m in the $(\partial D/\partial E)/\varepsilon_0$ curve when the polarization field was 200 MV/m. At higher polarization fields (> 200 MV/m), space charges were accumulated and thus oriented dipoles were stabilized (or saturated). After removal of the applied electric field, remnant polarization was relatively high in film D. The schematic of poling and discharge processes for the film D is shown in the inset of Figure 10A.

A summary of the maximum displacement (D_{max}) and remnant displacement (D_{rem}) for films A, B, and D as a function of polarization field is shown in Figure 11. The D_{max} and the D_{rem} of the film A were the lowest and increased monotonically with the polarization field. The D_{max} and the D_{rem} of the film B were the highest and increased sharply between 100 and 200 MV/m. The D_{max} and the D_{rem} of film D were in between those for films A and B and increased gradually between 100 and 300 MV/m.

Phase Transformation at High Electric Fields. Figure 11 shows that upon high field poling and discharge processes there are clear differences among films A, B, and D. We speculate that there could be ferroelectric phase transformations induced by the high electric field poling. To study the phase transformation during the $D-E$ loop measurement, a cycled dc poling experiment with a 50 MV/m increment was conducted for films A, B, and D to simulate the poling processes in the $D-E$ loop study. The crystalline phases in the poled samples were immediately studied by FTIR and 1D WAXD to avoid dipole depolarization with time. For film A, no obvious changes were detected by FTIR (Figure 12A) and 1D WAXD (Figure 12B) measurements, suggesting that no obvious phase transformation occurred after electric poling up to ca. 300 MV/m, although the α-helical conformation might have changed from alternating up and down to uniformly up (or down), as reported before.[28]

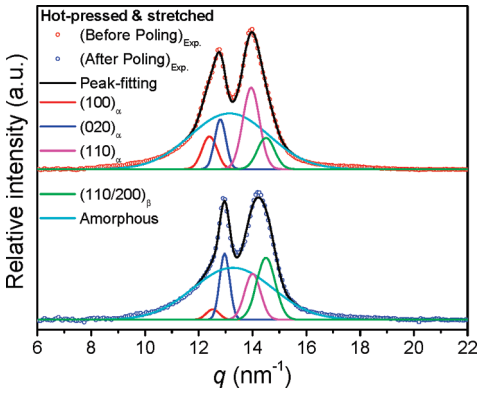

Figure 13. Peak fitting results of 1D WAXD profiles for the hot-pressed and stretched film D before and after the dc cycled poling process.

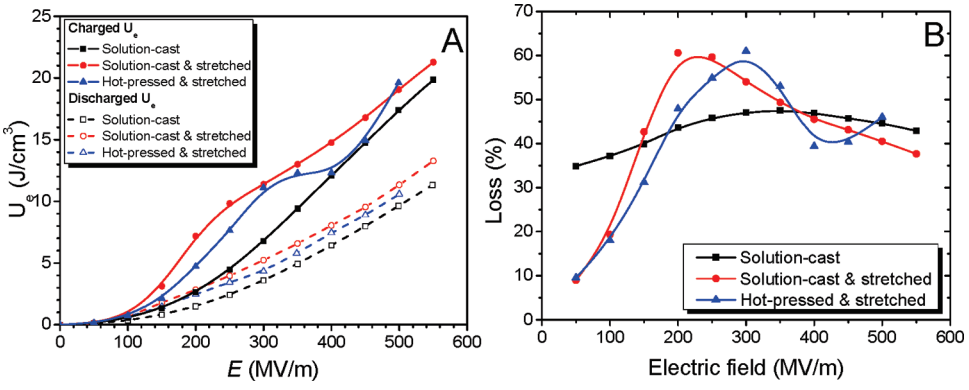

Figure 14. (A) Charged and discharged energy densities and (B) losses as a function of the applied electric fields for the solution-cast, solution-cast and stretched, and hot-pressed and stretched films A, B, and D, respectively.

For the solution-cast and stretched film B, also no substantial changes and phase transformation were found up to a poling field of 376 MV/m, as evidenced by nearly overlapped FTIR spectra in Figure 12A and 1D WAXD profiles in Figure 12B before and after the cycled dc poling process. However, this was not the case for the hot-pressed and stretched film D. After the cycled dc poling, the FTIR peak intensity of the α-crystal absorption bands at 614, 532, 486, and 410 cm^{-1} decreased in Figure 12A, and the WAXD reflection peaks slightly shifted to the right in Figure 12B. After peak fitting, results are shown in Figure 13 (and Table S3 in the Supporting Information) to quantify the relative contents of the α- and β-phases before and after the cycled dc poling process. About one-fourth of the α-crystals had already transformed to the β-crystals (7.3% before poling to 16.9% after poling) when the poling field was up to 286 MV/m. Therefore, we conclude that the difference between films B and D was likely a result of an easier phase transformation in film D than film B. In the future, more experiments are necessary to understand the exact mechanism for an easy phase transformation in film D.

Electric Energy Storage and Discharge Behaviors. The charged and discharged energy densities could be directly obtained from Figures 8A, 9A, and 10A. Results are shown in Figure 14A. First, the solution-cast film A had the lowest charged and discharged U_e because the largest dipole moments were oriented perpendicular to the applied electric field and could not be easily poled. The increases in charged and discharged U_e as a function of the electric field were gradual and monotonic. Second, the solution-cast and stretched film B had the highest charged and discharged U_e. Interestingly, the charged U_e had a sharp increase around 150 MV/m and then had a nearly linear increase after 250 MV/m. Third, the charged and discharged U_e of the hot-pressed and stretched film D were in between those of the films A and B. Similarly, the charged U_e for the film D had a relatively sharp increase between 150 and 300 MV/m and leveled off until 400 MV/m, after which it increased again. The sharp increases in the charged U_e for the films B and D between 100 and 300 MV/m coincided well with the peaks in the $(\partial D/\partial E)/\varepsilon_0$ curve in Figures 8B and 9B. Clearly, the increase in the charged U_e indicated that space charges were accumulated in the samples when the mobile dipoles started to orient along the applied electric field in order to stabilize them.

Although induced space charges enhanced the electric energy storage, they could not be easily discharged from the samples for practical uses during fast pulses.[20] This is reflected by the much lower discharged U_e for the films A, B, and D. Here, we define the loss as $[1 - U_e(\text{discharged})/U_e(\text{charged})]$, which includes both ferroelectric and conduction losses.[12] Figure 14B shows the losses for the films A, B, and D as a function of the electric field. The loss curves for films A, B, and D showed maxima around 350 MV/m (47% loss), 200 MV/m (61% loss), and 300 MV/m (62% loss), after which the losses started to decrease. At relatively low field (< 150 MV/m), the film A had much higher loss than films B and D. This corresponded well with the low field dielectric loss ($\tan\delta$) study in Figure 7B and could be attributed to the molecular motion accompanied by the change of dipole moment along the chain direction in α-crystals. Between 150 and 350 MV/m, films B and D had higher losses than the film A. After 400 MV/m, all films exhibited losses between 38% and 46%. Note that the discharged U_e for films A, B, and D (11−13.5 J/cm^3 at 600 MV/m) are much higher than that of BOPP (4.88 J/cm^3 at 700 MV/m).

Conclusions

In conclusion, PVDF crystals with different orientations in P(VDF−HFP) films were obtained by varying film fabrication and processing conditions. Anisotropic dielectric constants and electric energy storages were observed. Films with crystal *c*-axes perpendicular to the electric field exhibited higher dielectric constants and higher electric energy densities than the film with its crystal *c*-axes parallel to the electric field. This was primarily attributed to the anisotropic orientational polarizability of PVDF crystals. At high electric fields, the anisotropic orientational polarizability resulted in higher maximum/remnant polarization and a lower dipole switching field in the films with the crystal *c*-axes perpendicular to the electric field than in the film with the crystal *c*-axes parallel to the electric field. This study provided physical insights for the practical application of ferroelectric polymers for advanced dielectric capacitor applications.

Acknowledgment. The authors are indebted to Prof. Steven Boggs at University of Connecticut and Prof. Jerome Lando at Case Western Reserve University for helpful discussions. This work is supported by ONR (N00014-05-1-0338) and NSF (DMR-0907580).

Supporting Information Available: DSC thermograms for P(VDF−HFP) copolymer films fabricated with different processing methods, frequency of FTIR absorbance spectra and potential energy distribution (PED) for PVDF crystals in α- and β-phases, calculation results of crystallinity and actual contents of α- and β-crystals in films A−D, calculation results of actual contents of α- and β-crystals in the film D before and after electric poling. This material is available free of charge via the Internet at http://pubs.acs.org.

References and Notes

(1) Lovinger, A. J. *Science* **1983**, *220*, 1115–1121.
(2) Tashiro, K. Crystal Structure and Phase Transition of PVDF and Related Copolymers. In *Ferroelectric Polymers: Chemistry, Physics, and Applications*, 1st ed.; Nalwa, H. S., Ed.; Marcel Dekker: New York, 1995; pp 63−182.
(3) Lu, Y.; Claude, J.; Neese, B.; Zhang, Q. M.; Wang, Q. *J. Am. Chem. Soc.* **2006**, *128*, 8120–8121.
(4) Lu, Y.; Claude, J.; Zhang, Q. M.; Wang, Q. *Macromolecules* **2006**, *39*, 6962–6968.
(5) Karawasa, N.; Goddard, W. A.III *Macromolecules* **1992**, *25*, 7268–7281.
(6) Chu, B.; Zhou, X.; Ren, K.; Neese, B.; Lin, M.; Wang, Q.; Bauer, F.; Zhang, Q. M. *Science* **2006**, *313*, 1887–1887.
(7) Tan, Q.; Irwin, P.; Cao, Y. *IEEJ Trans. FM* **2006**, *126*, 1152–1159.
(8) Ho, J.; Ramprasad, R.; Boggs, S. *IEEE Trans. Dielectr. Electr. Insul.* **2007**, *14*, 1295–1301.
(9) Starkweather, J., H. W.; Avakian, P.; Matheson, J., R. R.; Fontanella, J. J.; Wintersgill, M. C. *Macromolecules* **1992**, *25*, 6871–6875.
(10) Xu, H.; Shen, D.; Zhang, Q. *Polymer* **2007**, *48*, 2124–2129.
(11) Jow, T. R.; Cygan, P. J. *J. Appl. Phys.* **1993**, *73*, 5147–5151.
(12) Zhou, X.; Chu, B.; Neese, B.; Lin, M.; Zhang, Q. M. *IEEE Trans. Dielectr. Electr. Insul.* **2007**, *14*, 1133–1138.
(13) Zhou, X.; Zhao, X.; Suo, Z.; Zou, C.; Runt, J.; Liu, S.; Zhang, S.; Zhang, Q. M. *Appl. Phys. Lett.* **2009**, *94*, 162901.
(14) Mizutani, T.; Yamada, T.; Ieda, M. *J. Phys. D: Appl. Phys.* **1981**, *14*, 1139–1147.
(15) Furukawa, T.; Lovinger, A. J.; Davis, G. T.; Broadhurst, M. G. *Macromolecules* **1983**, *16*, 1885–1890.
(16) Furukawa, T. *Phase Transitions* **1989**, *18*, 143–211.
(17) Furukawa, T.; Nakajima, K.; Koizumi, T.; Date, M. *Jpn. J. Appl. Phys.* **1987**, *26*, 1039–1045.
(18) Samara, G. A. *J. Phys.: Condens. Matter* **2003**, *15*, R367–R411.
(19) Ranjan, V.; Yu, L.; Nardelli, M. B.; Bernholc, J. *Phys. Rev. Lett.* **2007**, *99*, 047801.
(20) Guan, F.; Yuan, Z.; Shu, E. W.; Zhu, L. *Appl. Phys. Lett.* **2009**, *94*, 052907.

(21) von Seggern, H.; Fedosov, S. N. *Appl. Phys. Lett.* **2002**, *81*, 2830–2832.
(22) Blythe, A. R. *Electrical Properties of Polymers*; Cambridge University Press: Cambridge, 1979; pp 15−37.
(23) Moon, S. E.; Kim, E. K.; Kwak, M. H.; Ryu, H. C.; Kim, Y. T.; Kang, K. Y.; Lee, S. J.; Kim, W. J. *Appl. Phys. Lett.* **2003**, *83*, 2166–2168.
(24) Cho, T. H.; Lee, J. K.; Ho, P. S.; Ryan, E. T.; Pellerin, J. G. *J. Vac. Sci. Technol., B* **2000**, *18*, 208–215.
(25) Boyd, R. H. *Macromolecules* **1984**, *17*, 217–221.
(26) Marcus, M. A. *IEEE Trans. Electr. Insul.* **1986**, *EI-21*, 519–523.
(27) Gregorio, R. Jr.; Ueno, E. M. *J. Mater. Sci., Lett.* **1999**, *34*, 4489–4500.
(28) Newman, B. A.; Scheinbeim, J. I. *Macromolecules* **1983**, *16*, 60–68.
(29) Klein, R. J.; Runt, J.; Zhang, Q. M. *Macromolecules* **2003**, *36*, 7220–7226.
(30) Kobayashi, M.; Tashiro, K.; Tadokoro, K. *Macromolecules* **1975**, *8*, 158–171.
(31) Bachmann, M. A.; Gordon, W. L.; Koenig, J. L.; Lando, J. B. *J. Appl. Phys.* **1979**, *50*, 6106–6112.
(32) Young, R. J.; Lovell, P. A. *Introduction to Polymers*, 2nd ed.; Nelson Rhornes: Cheltenham, 1991; pp 310−428.
(33) Matsushige, K.; Nagata, K.; Imada, S.; Takemura, T. *Polymer* **1980**, *21*, 1391–1397.
(34) Furukawa, T.; Wang, T. Measurements and Properties of Ferroelectric Polymers. In *The Applications of Ferroelectric Polymers*; Wang, T., Herbert, J. M., Glass, A. M., Eds.; Chapman and Hall: New York, 1988; Vol. *5*, pp 66−117.
(35) Hahn, B.; Wendorff, J.; Yoon, D. Y. *Macromolecules* **1985**, *18*, 718–721.
(36) Takahashi, Y.; Kodama, H.; Nakamura, M.; Furukawa, T.; Date, M. *Polym. J.* **1999**, *31*, 263–267.
(37) Furukawa, T.; Date, M.; Fukada, E. *J. Appl. Phys.* **1980**, 1135–1141.
(38) Lu, Y.; Claude, J.; Norena-Franco, L. E.; Wang, Q. *J. Phys. Chem. B* **2008**, *112*, 10411–10416.
(39) Pfister, G.; Abkowitz, M.; Crystal, R. G. *J. Appl. Phys.* **1973**, *44*, 2064–2071.
(40) Mizutani, T.; Nagata, T.; Ieda, M. *J. Phys. D: Appl. Phys.* **1984**, *17*, 1883–1887.
(41) Butenko, A. F.; Fedosov, S. N.; Sergeeva, A. E. *Trapping of compensating charges in corona poled PVDF films*. [Online] **2009**, arXiv:0704.3449. arXiv.org e-Print. http://arxiv.org/abs/0704.3449 (accessed Aug 1, 2009).
(42) Fedosov, S. N.; von Seggern, H. *J. Appl. Phys.* **2008**, *103*, 014105.